Intelligent Reflecting Surface-Aided SWIPT: Joint Waveform, Active and Passive Beamforming Design

Yang Zhao, *Member, IEEE,* Bruno Clerckx, *Senior Member, IEEE,* and Zhenyuan Feng, *Member, IEEE*

Abstract—The performance of Simultaneous Wireless Information and Power Transfer (SWIPT) is mainly constrained by the received Radio-Frequency (RF) signal strength. To tackle this problem, we introduce an Intelligent Reflecting Surface (IRS) to compensate the propagation loss and boost the transmission efficiency. This paper proposes a novel IRS-aided SWIPT system where a multi-carrier multi-antenna Access Point (AP) transmits information and power simultaneously to a single-antenna User Equipment (UE) under the assist of an IRS. Considering energy harvester nonlinearity and practical transceiving strategies, we characterize the achievable Rate-Energy (R-E) region through a joint design of waveform, active and passive beamforming based on the Channel State Information at the Transmitter (CSIT). This non-convex problem is then solved by the Block Coordinate Descent (BCD) method, where the active precoder is obtained in a closed form, the passive beamformer is optimized by the Successive Convex Approximation (SCA) approach, and the waveform is designed by the Geometric Programming (GP) technique. Since the computational complexity of the GP-based algorithm scales exponentially with the number of subbands, we also propose two low-complexity adaptive waveform design to facilitate practical SWIPT implementation. Simulation results show considerable R-E gain over benchmark schemes and demonstrate the importance of accounting harvester nonlinearity in the passive beamforming design.

Index Terms—Simultaneous wireless information and power transfer, intelligent reflecting surface, waveform design, beamforming design, energy harvester nonlinearity.

I. INTRODUCTION

A. Simultaneous Wireless Information and Power Transfer

WITH the great advance in communication performance, a bottleneck of wireless networks has come to energy supply. Simultaneous Wireless Information and Power Transfer (SWIPT) is a promising solution to connect and power mobile devices via electromagnetic (EM) waves in the Radio-Frequency (RF) band. It provides low power at μW level but broad coverage up to hundreds of meters in a sustainable and controllable manner, bringing more opportunities to the Internet of Things (IoT) and Machine to Machine (M2M) networks. The upsurge in the number of wireless devices, together with the decrease of electronics power consumption, calls for a re-thinking of future wireless networks based on Wireless Power Transfer (WPT) and SWIPT [1].

The concept of SWIPT was first cast in [2], where the authors investigated the Rate-Energy (R-E) tradeoff for a flat Gaussian channel and typical discrete channels. [3] proposed

two practical co-localized information and power receivers, i.e. Time Switching (TS) and Power Splitting (PS). Dedicated information and energy beamforming were then investigated in [4], [5] to characterize the R-E region for multi-antenna broadcast and interference channels. On the other hand, [6] pointed out that the RF-to-Direct Current (DC) conversion efficiency of rectifiers depends on the input power and waveform shape. It implies that the modeling of the energy harvester, in particular its nonlinearity, has a crucial and significant impact on the waveform preference, resource allocation and system design of any wireless-powered systems [1], [6], [7]. Motivated by this, [8] derived a tractable nonlinear harvester model based on the Taylor expansion of diode I-V characteristics, then performed joint waveform and beamforming design for WPT. Simulation and experiments showed the benefit of modeling energy harvester nonlinearity in real system design [9], [10] and demonstrated the joint waveform and beamforming strategy as a key technique to expand the operation range [11]. A low-complexity adaptive waveform design by Scaled Matched Filter (SMF) was proposed in [12] to exploit the rectifier nonlinearity, whose advantage is then demonstrated in a prototype with channel acquisition [13]. Beyond WPT, [14] uniquely showed that the rectifier nonlinearity brings radical changes to SWIPT design, namely 1) modulated and unmodulated waveforms are not equally suitable for wireless power delivery, 2) a multi-carrier unmodulated waveform superposed to a multi-carrier modulated waveform can enlarge the R-E region of SWIPT, 3) a combination of PS and TS is generally the best strategy, 4) the optimal input distribution is not the conventional Circularly Symmetric Complex Gaussian (CSCG), 5) the rectifier nonlinearity is beneficial to system performance and is essential to efficient SWIPT design. Those observations, validated experimentally in [9], led to the question: *What is the optimal input distribution for SWIPT under nonlinearity?* This question was answered in [15] for single-carrier SWIPT, and some attempts were further made in [16] for multi-carrier SWIPT. The answer sheds new light to fundamental limits of SWIPT and practical signaling (e.g. modulation and waveform) strategies. It is now well understood from [14]–[16] that, due to the nonlinearity, a combination of CSCG and on-off keying in single-carrier setting and non-zero mean asymmetric inputs in multi-carrier setting lead to significantly larger R-E region compared to conventional CSCG. Recently, [17] used machine learning techniques to design SWIPT signaling under nonlinearity to complement the information-theoretic results of [15], and new modulation schemes were subsequently invented.

The authors are with the Department of Electrical and Electronic Engineering, Imperial College London, London SW7 2AZ, U.K. (e-mail: {yang.zhao18, b.clerckx, zhenyuan.feng19}@imperial.ac.uk).

B. Intelligent Reflecting Surface

Intelligent Reflecting Surface (IRS) has recently emerged as a promising technique that adapts the propagation environment to enhance the spectrum and energy efficiency. In practice, an IRS consists of multiple individual reflecting elements to adjust the amplitude and phase of the incoming signal for a smart reflection (i.e. passive beamforming). Different from relay, backscatter and Frequency-Selective Surface (FSS) [18], IRS adaptively assists the primary transmission by passive components to suppress thermal noise but is limited to frequency-dependent reflection.

Inspired by the development of real-time reconfigurable meta-materials [19], the authors of [20] introduced a programmable metasurface that steers or polarizes the EM wave at a specific frequency to mitigate signal attenuation. Motivated by this, [21] proposed an IRS-assisted Multiple-Input Single-Output (MISO) system and jointly optimized the precoder at the Access Point (AP) and the phase shifts at the IRS to minimize the transmit power. The active and passive beamforming problem was then extended to the discrete phase shift case [22] and the multi-user case [23]. In [24], the authors investigated the impact of non-zero resistance on the reflection pattern and emphasized the dependency of the reflection amplitude on the phase shift for practical IRS. To estimate the cascaded AP-IRS-User Equipment (UE) link without RF-chains at the IRS, practical protocols based on element-wise on/off switching [25], reflection pattern design [26], [27], and compressed sensing [28] have been proposed. [29] considered a novel dynamic passive beamforming for Orthogonal Frequency-Division Multiplexing (OFDM) systems, where the reflection coefficient is varied over consequent time slots to enable flexible resource allocation over time-frequency Resource Blocks (RBs). In [30], a prototype IRS with 256 2-bit elements based on Positive Intrinsic-Negative (PIN) diodes was developed to support real-time high-definition video transmission at GHz and mmWave frequency.

C. IRS-Aided SWIPT

The effective channel enhancement and low power consumption of IRS are expected to bring more opportunities to SWIPT. For a multi-user IRS-aided SWIPT system, dedicated energy beams are proved unnecessary for the Weighted Sum-Power (WSP) maximization problem [31] but essential when fairness issue is considered [32]. It was also demonstrated in [33] that Line-of-Sight (LoS) links can boost the WSP because rank-deficient channels require less energy beams. However, the above papers only consider single-carrier transmission based on inaccurate linear energy harvester model. Motivated by this, we marry the benefits of joint multi-carrier waveform and active beamforming optimization for SWIPT (accounting for nonlinearity) with the passive beamforming capability of IRS in this paper. We ask ourselves the important question: *How to jointly exploit the spatial domain and the frequency domain efficiently through joint waveform and beamforming design to enlarge as much as possible the R-E region of IRS-aided SWIPT?* The contributions of this paper are summarized as follows.

First, we propose a novel IRS-aided SWIPT architecture based on joint waveform, active and passive beamforming design. To elevate the rectifier nonlinearity, we superpose a multi-carrier unmodulated power waveform (deterministic multisine) to a multi-carrier modulated information waveform and evaluate the performance under TS and PS modes. The proposed joint waveform, active and passive beamforming architecture exploits rectifier nonlinearity, beamforming gain and channel selectivity across spatial and frequency domains to enlarge the achievable R-E region. This is the first paper to tackle energy harvester nonlinearity, multi-carrier transmission, and co-localized receiver for IRS-aided SWIPT.

Second, we characterize the achievable R-E region with multiple energy maximization problems with different rate constraints, and solve each R-E boundary point by an Block Co-ordinate Descent (BCD) algorithm based on the Channel State Information at the Transmitter (CSIT). For active beamforming, we prove that the global optimal active information and power precoders coincide at Maximum-Ratio Transmission (MRT) under rectifier nonlinearity. For passive beamforming, we propose a Successive Convex Approximation (SCA) algorithm that obtains the IRS reflection coefficient by relax-then-extract method. Finally, the superposed waveform is optimized by the Geometric Programming (GP) technique. Numerical results demonstrate the strict convergence of the proposed BCD algorithm under various configurations.

Third, we introduce two low-complexity adaptive waveform design to avoid the exponential complexity of the GP algorithm. The Water-Filling (WF) strategy for modulated waveform and SMF strategy for multisine waveform are combined under TS and PS setups to facilitate practical SWIPT implementation.

Fourth, we provide numerical results to evaluate the performance of the proposed algorithms. It is concluded that 1) multisine waveform is beneficial to multi-carrier energy transfer especially when the number of subbands is large, 2) TS is preferred at low Signal-to-Noise Ratio (SNR) while PS is preferred at high SNR, 3) there exist two optimal IRS development locations, one close to the AP and one close to the UE, 4) the SNR scales linearly with the number of transmit antennas and quadratically with the number of IRS elements, 5) due to rectifier nonlinearity, the output DC current scales quadratically with the number of transmit antennas and quartically with the number of IRS elements, 6) Wireless Information Transfer (WIT) and WPT prefer different passive beamforming especially when the bandwidth is large. These observations demonstrate the advantage of the proposed IRS-aided SWIPT architecture and emphasize the importance of accounting harvester nonlinearity in the system design.

Fifth, since the IRS is generally passive and with finite reflection states, we investigate the influence of imperfect CSIT and quantized IRS on overall R-E behavior. The adaptive algorithms are proved robust and effective under different channel estimation errors, and only ? quantization bits are required for each IRS element to provide a decent performance.

Organization: Section II introduces the system model, transceiving mode and rectifier nonlinearity. Section III formulates the problem and tackles the waveform, active and passive beamforming optimization. Section IV presents the simulation
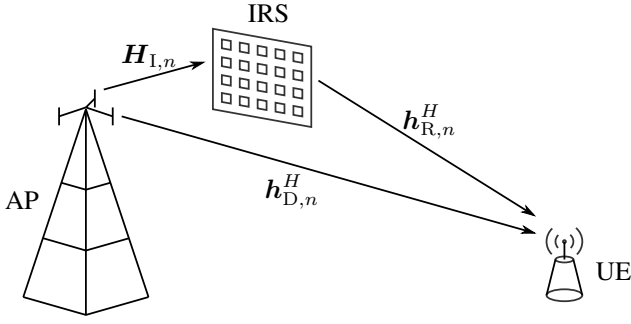
Fig. 1. An IRS-aided multi-carrier SWIPT system.

results and evaluates the proposed algorithms. Section V concludes the paper.

Notations: Scalars, vectors and matrices are denoted respectively by italic, bold lower-case and bold upper-case letters. j denotes the imaginary unit. $\mathbb{C}^{x \times y}$ denotes the subspace spanned by complex $x \times y$ matrices. $\Re\{\cdot\}$ and $\Im\{\cdot\}$ denote respectively the real and imaginary part of a complex entity. $(\cdot)^*$, $(\cdot)^T$, $(\cdot)^H$, $(\cdot)^+$, $|\cdot|$, $\|\cdot\|$ represent respectively the conjugate, transpose, conjugate transpose, ramp function, absolute value, and Euclidean norm operators. $\arg(\cdot)$, $\mathrm{rank}(\cdot)$, $\mathrm{Tr}(\cdot)$, $\mathrm{diag}(\cdot)$ denote the argument, rank, trace, and a square matrix with input elements on the main diagonal. $S \succeq 0$ means S is positive semi-definite. $\mathbb{A}\{\cdot\}$ extracts the DC component of a signal. $\mathbb{E}_X\{\cdot\}$ takes expectation with respect to random variable X (X is omitted for simplicity). The distribution of a CSCG random vector with mean $\mathbf{0}$ and covariance Σ is denoted by $\mathcal{CN}(\mathbf{0}, \Sigma)$. $\sim$ means "distributed as". $(\cdot)^\star$ and $(\cdot)^{(i)}$ denote respectively the stationary value and the value at iteration i.

II. SYSTEM MODEL

As shown in Fig. 1, we propose an IRS-aided SWIPT system where a M-antenna AP delivers information and power simultaneously, through a L-element IRS, to a single-antenna UE over N orthogonal evenly-spaced subbands. We consider quasi-static block fading and assume the CSIT of AP-UE and AP-IRS-UE cascaded channels are given. The signals reflected by two or more times are omitted and the noise power is assumed too small to be harvested.

A. Transmitted Signal

Denote $\tilde{x}_{\mathrm{I},n} \sim \mathcal{CN}(0,1)$ as the information symbol transmitted over subband $n \in \{1, \ldots, N\}$. The superposed signal transmitted on antenna $m \in \{1, \ldots, M\}$ at time t is

$$x_m(t) = \Re\left\{\sum_{n=1}^{N}\left(w_{\mathrm{I},n,m}\tilde{x}_{\mathrm{I},n}(t) + w_{\mathrm{P},n,m}\right)e^{j2\pi f_n t}\right\} \quad (1)$$

where $w_{\mathrm{I/P},n,m}$ denotes the complex weight of the modulated/multisine waveform transmitted at subband n on antenna m, and f_n is the frequency of subband n. On top of this, we

stack up $\boldsymbol{w}_{\mathrm{I/P},n} \triangleq [w_{\mathrm{I/P},n,1}, \ldots, w_{\mathrm{I/P},n,M}]^T \in \mathbb{C}^{M \times 1}$ and $\boldsymbol{x}(t) \triangleq [x_1(t), \ldots, x_M(t)]^T \triangleq \boldsymbol{x}_{\mathrm{I}}(t) + \boldsymbol{x}_{\mathrm{P}}(t) \in \mathbb{C}^{M \times 1}$, where

$$\boldsymbol{x}_{\mathrm{I}}(t) = \Re\left\{\sum_{n=1}^{N} \boldsymbol{w}_{\mathrm{I},n}\tilde{x}_{\mathrm{I},n}(t)e^{j2\pi f_n t}\right\}, \quad (2)$$

$$\boldsymbol{x}_{\mathrm{P}}(t) = \Re\left\{\sum_{n=1}^{N} \boldsymbol{w}_{\mathrm{P},n}e^{j2\pi f_n t}\right\} \quad (3)$$

are the modulated and multisine components, respectively.

B. Reflection Pattern and Composite Channel

According to Green's decomposition [34], the backscattered signal of an antenna can be decomposed into the *structural mode* component and the *antenna mode* component. The former is fixed for a given antenna and can be regarded as part of the environment multipath, while the latter is adjustable and depends on the mismatch of the antenna and load impedances. IRS element $l \in \{1, \ldots, L\}$ varies its impedance $Z_l = R_l + jX_l$ in a fully passive manner to reflect the incoming signal, and the reflection coefficient is defined as

$$\phi_l = \frac{Z_l - Z_0}{Z_l + Z_0} \triangleq \eta_l e^{j\theta_l} \quad (4)$$

where Z_0 is the characteristic impedance, $\eta_l \in [0, 1]$ is the reflection amplitude, and $\theta_l \in [0, 2\pi)$ is the phase shift [1]. We also define $\boldsymbol{\Theta} \triangleq \mathrm{diag}(\phi_1, \ldots, \phi_L) \in \mathbb{C}^{L \times L}$ as the IRS matrix and let $\boldsymbol{\phi} \triangleq [\phi_1, \ldots, \phi_L]^H \in \mathbb{C}^{L \times 1}$ be the IRS vector [2].

Remark 1. *The element impedance Z_l maps to the reflection coefficient ϕ_l uniquely. Since the reactance X_l depends on the frequency, the reflection coefficient ϕ_l is also a function of frequency and cannot be designed independently at different subbands. In this paper, we assume the bandwidth is incomparable to the operating frequency such that the reflection coefficients of each IRS element are the same at all subbands. That is to say, ϕ_l is shared by M auxiliary channels over N subbands.*

At subband n, we denote the AP-UE direct channel as $\boldsymbol{h}_{\mathrm{D},n}^H \in \mathbb{C}^{1 \times M}$, AP-IRS incident channel as $\boldsymbol{H}_{\mathrm{I},n} \in \mathbb{C}^{L \times M}$, and IRS-UE reflective channel as $\boldsymbol{h}_{\mathrm{R},n}^H \in \mathbb{C}^{1 \times L}$. The auxiliary link provided by the IRS can be modeled as a concatenation of the incident channel, the IRS reflection, and the reflective channel. Hence, the composite equivalent channel reduces to

$$\boldsymbol{h}_n^H = \boldsymbol{h}_{\mathrm{D},n}^H + \boldsymbol{h}_{\mathrm{R},n}^H\boldsymbol{\Theta}\boldsymbol{H}_{\mathrm{I},n} = \boldsymbol{h}_{\mathrm{D},n}^H + \boldsymbol{\phi}^H\boldsymbol{V}_n \quad (5)$$

where we define the cascaded AP-IRS-UE channel (without IRS reflection) as $\boldsymbol{V}_n \triangleq \mathrm{diag}(\boldsymbol{h}_{\mathrm{R},n}^H)\boldsymbol{H}_{\mathrm{I},n} \in \mathbb{C}^{L \times M}$.

---

[1] Due to the non-zero power consumption at the IRS, practically $R_l > 0$ such that $\eta_l < 1$ and depends on θ_l. This paper sticks to the commonest and simplest IRS model where the reflection coefficient is assumed unit.

[2] Note the conjugate transpose in the notation of $\boldsymbol{\phi}$ makes its entries the complex conjugate of the diagonal entries of $\boldsymbol{\Theta}$.

C. Received Signal

The total received signal at the single-antenna UE can be decomposed as $y(t) \triangleq y_{\mathrm{I}}(t) + y_{\mathrm{P}}(t)$, where

$$y_{\mathrm{I}}(t) = \Re \left\{ \sum_{n=1}^{N} \boldsymbol{h}_n^H \boldsymbol{w}_{\mathrm{I},n} \tilde{x}_{\mathrm{I},n}(t) e^{j2\pi f_n t} \right\}, \quad (6)$$

$$y_{\mathrm{P}}(t) = \Re \left\{ \sum_{n=1}^{N} \boldsymbol{h}_n^H \boldsymbol{w}_{\mathrm{P},n} e^{j2\pi f_n t} \right\} \quad (7)$$

capture the contribution of modulated and multisine waveforms over all subbands. Note that $y_{\mathrm{I}}(t)$ can also be used for energy harvesting if necessary, but $y_{\mathrm{P}}(t)$ is unmodulated and cannot be used for information purpose.

D. Transceiving Modes

Consider TS and PS as two practical transceiving modes for SWIPT. TS relies on perfect clock synchronization, where the transmitter divides each slot into dedicated data session with length $1-\eta$ and energy session with length η, then designs the waveform for WIT and WPT independently. At the receiver, only information decoder or energy harvester is activated at a time. Varying η from 0 to 1 corresponds to a R-E segment from the WIT point to the WPT point.

On the other hand, the PS waveform consists of modulated and multisine components, and the receiver splits the incoming signal into individual data stream with power ratio $1-\rho$ and energy stream with power ratio ρ. Note that in PS the splitting ratio ρ and the superposed waveform require a joint design, but in TS the duration ratio η is irrelevant to the waveform design in both sessions. Therefore, we focus on PS in the following context since TS can be regard as a special case (a time sharing between WIT and WPT).

E. Information Decoder

A major benefit of the superposed waveform is that the multisine is deterministic and creates no interference to the modulated waveform. Therefore, the achievable rate writes as

$$R(\boldsymbol{\phi}, \boldsymbol{w}_{\mathrm{I}}, \rho) = \sum_{n=1}^{N} \log_2 \left(1 + \frac{(1-\rho)|\boldsymbol{h}_n^H \boldsymbol{w}_{\mathrm{I},n}|^2}{\sigma_n^2} \right) \quad (8)$$

where σ_n^2 is the variance of the total noise (at RF-band and during RF-to-baseband conversion) on tone n. Rate (8) is achievable with either waveform cancellation or translated demodulation [14].

F. Energy Harvester

In this section, we briefly revisit a tractable nonlinear rectenna model that relates the harvester output DC current to the received signal. Fig. 2a illustrates the equivalent circuit of an ideal antenna, where the antenna has an impedance R_{A} and the incoming signal creates an voltage source $v_{\mathrm{S}}(t)$. Let R_{in} be the total input impedance of the rectifier and matching network, and we assume the voltage across the matching network is negligible. When perfectly matched ($R_{\mathrm{in}} = R_{\mathrm{A}}$), the rectifier input voltage is $v_{\mathrm{in}}(t) = y(t)\sqrt{\rho R_{\mathrm{A}}}$.

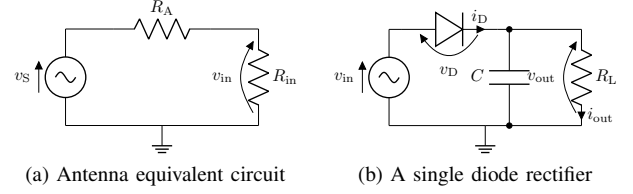(a) Antenna equivalent circuit   (b) A single diode rectifier

Fig. 2. Receive antenna and energy harvester circuits.

Rectifiers consist of nonlinear components as diode and capacitor to produce DC output and store energy [35]. Consider a simplified rectifier model in Fig. 2b where a single series diode is followed by a low-pass filter with a parallel load. As detailed in [8], [14], a truncated Taylor expansion of the diode I-V characteristic equation suggests that, when the subband frequencies are evenly-spaced, maximizing the average output DC current is equivalent to maximizing a monotonic function [3]

$$z(\boldsymbol{\phi}, \boldsymbol{w}_{\mathrm{I}}, \boldsymbol{w}_{\mathrm{P}}, \rho) = \sum_{i \, \mathrm{even}, i \geq 2}^{n_0} k_i \rho^{i/2} R_{\mathrm{A}}^{i/2} \mathbb{E} \left\{ \mathbb{A} \left\{ y(t)^i \right\} \right\} \quad (9)$$

where n_0 is the truncation order and $k_i \triangleq i_{\mathrm{S}}/i!(n'v_{\mathrm{T}})^i$ is the diode coefficient (i_{S} is the reverse bias saturation current, n' is the diode ideality factor, v_{T} is the thermal voltage). With a slight abuse of notation, we refer to z as the average output DC current in the following context. It can be observed that the traditional linear harvester model, where the output DC power equals the sum of the power harvested on each frequency, is a special case of (9) with $n_0 = 2$. However, due to the coupling effect among different frequencies, some high-order AC components compensate each other and further contribute to the output DC power. In other words, even-order terms with $i \geq 4$ account for the diode nonlinear behavior. For simplicity, we choose $n_0 = 4$ to investigate the fundamental rectifier nonlinearity, and define $\beta_2 \triangleq k_2 R_{\mathrm{A}}$, $\beta_4 \triangleq k_4 R_{\mathrm{A}}^2$ to rewrite z by (10). Note that $\mathbb{E}\left\{|\tilde{x}_{\mathrm{I},n}|^2\right\} = 1$ but $\mathbb{E}\left\{|\tilde{x}_{\mathrm{I},n}|^4\right\} = 2$, which can be interpreted as a modulation gain on the nonlinear terms of the output DC current. Inspired by [36], we further stack $\boldsymbol{h} \triangleq [\boldsymbol{h}_1^T, \ldots, \boldsymbol{h}_N^T]^T \in \mathbb{C}^{MN \times 1}$, $\boldsymbol{w}_{\mathrm{I/P}} \triangleq [\boldsymbol{w}_{\mathrm{I/P},1}^T, \ldots, \boldsymbol{w}_{\mathrm{I/P},N}^T]^T \in \mathbb{C}^{MN \times 1}$, and define $\boldsymbol{W}_{\mathrm{I/P}} \triangleq \boldsymbol{w}_{\mathrm{I/P}} \boldsymbol{w}_{\mathrm{I/P}}^H \in \mathbb{C}^{MN \times MN}$. As illustrated by Fig. 3, $\boldsymbol{W}_{\mathrm{I/P}}$ can be divided into $N \times N$ blocks of size $M \times M$, and we let $\boldsymbol{W}_{\mathrm{I/P},k}$ keep its block diagonal $k \in \{-N+1, \ldots, N-1\}$ and set all other blocks to $\mathbf{0}^{M \times M}$. Hence, the components of z reduce to (11) – (14).

G. Rate-Energy Region

The achievable R-E region is defined as

$$C_{R_{\mathrm{ID}} - I_{\mathrm{EH}}}(P) \triangleq \left\{ (R_{\mathrm{ID}}, I_{\mathrm{EH}}) : R_{\mathrm{ID}} \leq R, I_{\mathrm{EH}} \leq z, \right.$$

$$\left. \frac{1}{2} \left(\|\boldsymbol{w}_{\mathrm{I}}\|^2 + \|\boldsymbol{w}_{\mathrm{P}}\|^2 \right) \leq P \right\} \quad (15)$$

where P is the average transmit power budget and $1/2$ converts the peak value to the average value.

---

[3]Note that this small-signal expansion model is only valid for the non-linear operation region of the diode, and the I-V relationship would be linear if the diode behavior is dominated by the load [8].

Fig. 3. $\boldsymbol{W}_{\text{I/P}}$ consists of $N \times N$ blocks of size $M \times M$. $\boldsymbol{W}_{\text{I/P},k}$ keeps the k-th block diagonal of $\boldsymbol{W}_{\text{I/P}}$ and nulls all remaining blocks. Solid, dashed and dotted blocks correspond to $k > 0$, $k = 0$ and $k < 0$, respectively. For $\boldsymbol{w}_{\text{I/P},n_1}\boldsymbol{w}_{\text{I/P},n_2}^H$, the k-th block diagonal satisfies $k = n_2 - n_1$.

III. PROBLEM FORMULATION

We characterize each R-E boundary point through a current maximization problem subject to transmit power, IRS magnitude, and rate constraint as

$$\max_{\boldsymbol{\phi}, \boldsymbol{w}_{\text{I}}, \boldsymbol{w}_{\text{P}}, \rho} z(\boldsymbol{\phi}, \boldsymbol{w}_{\text{I}}, \boldsymbol{w}_{\text{P}}, \rho) \tag{16a}$$

$$\text{s.t.} \quad \frac{1}{2}\left(\|\boldsymbol{w}_{\text{I}}\|^2 + \|\boldsymbol{w}_{\text{P}}\|^2\right) \leq P, \tag{16b}$$

$$R(\boldsymbol{\phi}, \boldsymbol{w}_{\text{I}}, \rho) \geq \bar{R}, \tag{16c}$$

$$|\phi_l| = 1, \quad l = 1, \ldots, L, \tag{16d}$$

$$0 \leq \rho \leq 1. \tag{16e}$$

Problem (16) is intricate with coupled variables in nonconvex expressions (16a), (16c), (16d). To obtain a feasible solution, we propose an BCD algorithm that iteratively updates 1) the IRS phase shift, 2) the active precoder, 3) the waveform amplitude and the splitting ratio, until convergence.

A. Passive Beamforming

In this section, we optimize the IRS phase shift $\boldsymbol{\phi}$ for any given waveform $\boldsymbol{w}_{\text{I/P}}$ and splitting ratio ρ. Note that

$$|\boldsymbol{h}_n^H \boldsymbol{w}_{\text{I},n}|^2 = \boldsymbol{w}_{\text{I},n}^H \boldsymbol{h}_n \boldsymbol{h}_n^H \boldsymbol{w}_{\text{I},n}$$

$$= \boldsymbol{w}_{\text{I},n}^H(\boldsymbol{h}_{\text{D},n} + \boldsymbol{V}_n^H\boldsymbol{\phi})(\boldsymbol{h}_{\text{D},n}^H + \boldsymbol{\phi}^H\boldsymbol{V}_n)\boldsymbol{w}_{\text{I},n}$$

$$= \boldsymbol{w}_{\text{I},n}^H \boldsymbol{M}_n^H \boldsymbol{\Phi} \boldsymbol{M}_n \boldsymbol{w}_{\text{I},n}$$

$$= \text{Tr}(\boldsymbol{M}_n \boldsymbol{w}_{\text{I},n} \boldsymbol{w}_{\text{I},n}^H \boldsymbol{M}_n^H \boldsymbol{\Phi})$$

$$= \text{Tr}(\boldsymbol{C}_n \boldsymbol{\Phi}) \tag{17}$$

where $\boldsymbol{M}_n \triangleq [\boldsymbol{V}_n^H, \boldsymbol{h}_{\text{D},n}]^H \in \mathbb{C}^{(L+1)\times M}$, t' is an auxiliary variable with unit modulus, $\bar{\boldsymbol{\phi}} \triangleq [\boldsymbol{\phi}^H, t']^H \in \mathbb{C}^{(L+1)\times 1}$, $\boldsymbol{\Phi} \triangleq \bar{\boldsymbol{\phi}}\bar{\boldsymbol{\phi}}^H \in \mathbb{C}^{(L+1)\times(L+1)}$, $\boldsymbol{C}_n \triangleq \boldsymbol{M}_n \boldsymbol{w}_{\text{I},n} \boldsymbol{w}_{\text{I},n}^H \boldsymbol{M}_n^H \in \mathbb{C}^{(L+1)\times(L+1)}$. On the other hand, we define $t_{\text{I/P},k}$ as

$$t_{\text{I/P},k} \triangleq \boldsymbol{h}^H \boldsymbol{W}_{\text{I/P},k} \boldsymbol{h}$$

$$= \text{Tr}(\boldsymbol{h}\boldsymbol{h}^H \boldsymbol{W}_{\text{I/P},k})$$

$$= \text{Tr}\left((\boldsymbol{h}_D + \boldsymbol{V}^H\boldsymbol{\phi})(\boldsymbol{h}_D^H + \boldsymbol{\phi}^H\boldsymbol{V})\boldsymbol{W}_{\text{I/P},k}\right)$$

$$= \text{Tr}(\boldsymbol{M}^H \boldsymbol{\Phi} \boldsymbol{M} \boldsymbol{W}_{\text{I/P},k})$$

$$= \text{Tr}(\boldsymbol{M} \boldsymbol{W}_{\text{I/P},k} \boldsymbol{M}^H \boldsymbol{\Phi})$$

$$= \text{Tr}(\boldsymbol{C}_{\text{I/P},k} \boldsymbol{\Phi}) \tag{18}$$

where $\boldsymbol{V} \triangleq [\boldsymbol{V}_1, \ldots, \boldsymbol{V}_N] \in \mathbb{C}^{L\times MN}$, $\boldsymbol{M} \triangleq [\boldsymbol{V}^H, \boldsymbol{h}_D]^H \in \mathbb{C}^{(L+1)\times MN}$, $\boldsymbol{C}_{\text{I/P},k} \triangleq \boldsymbol{M} \boldsymbol{W}_{\text{I/P},k} \boldsymbol{M}^H \in \mathbb{C}^{(L+1)\times(L+1)}$. On

$$z(\boldsymbol{\phi}, \boldsymbol{w}_{\text{I}}, \boldsymbol{w}_{\text{P}}, \rho) = \beta_2 \rho\Big(\mathbb{E}\big\{\mathbb{A}\{y_{\text{I}}^2(t)\}\big\} + \mathbb{A}\{y_{\text{P}}^2(t)\}\Big) + \beta_4 \rho^2\Big(\mathbb{E}\big\{\mathbb{A}\{y_{\text{I}}^4(t)\}\big\} + \mathbb{A}\{y_{\text{P}}^4(t)\} + 6\mathbb{E}\big\{\mathbb{A}\{y_{\text{I}}^2(t)\}\big\}\mathbb{A}\{y_{\text{P}}^2(t)\}\Big), \tag{10}$$

$$\mathbb{E}\big\{\mathbb{A}\{y_{\text{I}}^2(t)\}\big\} = \frac{1}{2}\sum_{n=1}^{N}(\boldsymbol{h}_n^H \boldsymbol{w}_{\text{I},n})(\boldsymbol{h}_n^H \boldsymbol{w}_{\text{I},n})^* = \frac{1}{2}\boldsymbol{h}^H \boldsymbol{W}_{\text{I},0}\boldsymbol{h}, \tag{11}$$

$$\mathbb{E}\big\{\mathbb{A}\{y_{\text{I}}^4(t)\}\big\} = \frac{3}{4}\left(\sum_{n=1}^{N}(\boldsymbol{h}_n^H \boldsymbol{w}_{\text{I},n})(\boldsymbol{h}_n^H \boldsymbol{w}_{\text{I},n})^*\right)^2 = \frac{3}{4}(\boldsymbol{h}^H \boldsymbol{W}_{\text{I},0}\boldsymbol{h})^2, \tag{12}$$

$$\mathbb{A}\{y_{\text{P}}^2(t)\} = \frac{1}{2}\sum_{n=1}^{N}(\boldsymbol{h}_n^H \boldsymbol{w}_{\text{P},n})(\boldsymbol{h}_n^H \boldsymbol{w}_{\text{P},n})^* = \frac{1}{2}\boldsymbol{h}^H \boldsymbol{W}_{\text{P},0}\boldsymbol{h}, \tag{13}$$

$$\mathbb{A}\{y_{\text{P}}^4(t)\} = \frac{3}{8}\sum_{\substack{n_1,n_2,n_3,n_4 \\ n_1+n_2=n_3+n_4}}(\boldsymbol{h}_{n_1}^H \boldsymbol{w}_{\text{P},n_1})(\boldsymbol{h}_{n_2}^H \boldsymbol{w}_{\text{P},n_2})(\boldsymbol{h}_{n_3}^H \boldsymbol{w}_{\text{P},n_3})^*(\boldsymbol{h}_{n_4}^H \boldsymbol{w}_{\text{P},n_4})^* = \frac{3}{8}\sum_{k=-N+1}^{N-1}(\boldsymbol{h}^H \boldsymbol{W}_{\text{P},k}\boldsymbol{h})(\boldsymbol{h}^H \boldsymbol{W}_{\text{P},k}\boldsymbol{h})^*. \tag{14}$$

top of this, (8) and (10) reduce to

$$R(\mathbf{\Phi}) = \sum_{n=1}^{N} \log_2 \left(1 + \frac{(1-\rho)\text{Tr}(\boldsymbol{C}_n \mathbf{\Phi})}{\sigma_n^2} \right), \qquad (19)$$

$$\begin{aligned} z(\mathbf{\Phi}) = &\frac{1}{2}\beta_2 \rho (t_{\text{I},0} + t_{\text{P},0}) \\ &+ \frac{3}{8}\beta_4 \rho^2 \left(2t_{\text{I},0}^2 + \sum_{k=-N+1}^{N-1} t_{\text{P},k} t_{\text{P},k}^* \right) \\ &+ \frac{3}{2}\beta_4 \rho^2 t_{\text{I},0} t_{\text{P},0}. \end{aligned} \qquad (20)$$

To maximize the non-concave expression (20), we propose a SCA algorithm and lower bound the second-order terms by their first-order Taylor expansions [37]. Based on the solution at iteration $i-1$, the approximations at iteration i are

$$(t_{\text{I},0}^{(i)})^2 \geq 2t_{\text{I},0}^{(i)} t_{\text{I},0}^{(i-1)} - (t_{\text{I},0}^{(i-1)})^2, \qquad (21)$$

$$t_{\text{P},k}^{(i)}(t_{\text{P},k}^{(i)})^* \geq 2\Re\left\{ t_{\text{P},k}^{(i)}(t_{\text{P},k}^{(i-1)})^* \right\} - t_{\text{P},k}^{(i-1)}(t_{\text{P},k}^{(i-1)})^*, \qquad (22)$$

$$\begin{aligned} t_{\text{I},0}^{(i)} t_{\text{P},0}^{(i)} &= \frac{1}{4}(t_{\text{I},0}^{(i)} + t_{\text{P},0}^{(i)})^2 - \frac{1}{4}(t_{\text{I},0}^{(i)} - t_{\text{P},0}^{(i)})^2 \\ &\geq \frac{1}{2}(t_{\text{I},0}^{(i)} + t_{\text{P},0}^{(i)})(t_{\text{I},0}^{(i-1)} + t_{\text{P},0}^{(i-1)}) \\ &\quad - \frac{1}{4}(t_{\text{I},0}^{(i-1)} + t_{\text{P},0}^{(i-1)})^2 - \frac{1}{4}(t_{\text{I},0}^{(i)} - t_{\text{P},0}^{(i)})^2 \end{aligned} \qquad (23)$$

Plugging (21) – (23) into (20), we obtain the DC current approximation (24) and transform problem (16) to

$$\max_{\mathbf{\Phi}} \quad \tilde{z}(\mathbf{\Phi}) \qquad (25\text{a})$$

$$\text{s.t.} \quad R(\mathbf{\Phi}) \geq \bar{R}, \qquad (25\text{b})$$

$$\mathbf{\Phi}_{l',l'} = 1, \quad l' = 1, \ldots, L+1, \qquad (25\text{c})$$

$$\mathbf{\Phi} \succeq 0, \qquad (25\text{d})$$

$$\text{rank}(\mathbf{\Phi}) = 1. \qquad (25\text{e})$$

Note that problem (25) is not a Semidefinite Programming (SDP) such that relaxing the rank constraint (25e) has no analytical performance guarantee. In Section IV, we prove through numerical simulations that the solution $\mathbf{\Phi}^\star$ to 25a – 25d is rank-1 under different configurations for all tested channel realizations. It suggests that the rank constraint (25e) can be dropped with negligible loss and $\bar{\phi}^\star$ can be obtained by eigen decomposition. In case $\mathbf{\Phi}^\star$ is not rank-1, a suboptimal solution can be extracted via the Gaussian randomization method [38]. Specifically, we decompose $\mathbf{\Phi}^\star = \boldsymbol{U}\boldsymbol{\Lambda}\boldsymbol{U}^H$, generate CSCG random vector $q \in \{1, \ldots, Q\}$ by $\boldsymbol{\xi}_q \sim \mathcal{CN}(\mathbf{0}, \boldsymbol{I}_{L+1})$, construct the candidate $\bar{\phi}_q = e^{j \arg(\boldsymbol{U}\boldsymbol{\Lambda}^{1/2}\boldsymbol{\xi}_q)}$, and choose the $\bar{\phi}^\star$ that maximizes (25a) as the solution. Finally, the

---

Algorithm 1 SCA: IRS Phase Shift.

1: **Input** $\beta_2, \beta_4, \boldsymbol{h}_{\text{D},n}, \boldsymbol{V}_n, \boldsymbol{w}_{\text{I/P},n}, \rho, \sigma_n, \bar{R}, Q, \epsilon, \forall n$
2: Construct $\boldsymbol{V}, \boldsymbol{M}, \boldsymbol{M}_n, \boldsymbol{C}_n, \boldsymbol{C}_{\text{I/P},k}, \forall n, k$
3: **Initialize** $i \leftarrow 0$, $\mathbf{\Phi}^{(0)}$
4: Get $t_{\text{I/P},k}^{(0)}, \forall k$ by (18)
5: **Repeat**
6:      $i \leftarrow i+1$
7:      Get $\mathbf{\Phi}^{(i)}$ by solving 25a – 25d
8:      Update $t_{\text{I/P},k}^{(i)}, \forall k$ by (18)
9:      Compute $z^{(i)}$ by (20)
10: **Until** $|z^{(i)} - z^{(i-1)}| \leq \epsilon$
11: Set $\mathbf{\Phi}^\star = \mathbf{\Phi}^{(i)}$
12: **If** $\text{rank}(\mathbf{\Phi}^\star) = 1$ **Then**
13:      Get $\bar{\phi}^\star$ by eigen decomposition, $\mathbf{\Phi}^\star = \bar{\phi}^\star(\bar{\phi}^\star)^H$
14: **Else**
15:      Get $\boldsymbol{U}, \boldsymbol{\Lambda}$ by eigen decomposition, $\mathbf{\Phi}^\star = \boldsymbol{U}\boldsymbol{\Lambda}\boldsymbol{U}^H$
16:      Generate $\boldsymbol{\xi}_q \sim \mathcal{CN}(\mathbf{0}, \boldsymbol{I}_{L+1}), \forall q$
17:      Construct $\bar{\phi}_q = e^{j \arg(\boldsymbol{U}\boldsymbol{\Lambda}^{1/2}\boldsymbol{\xi}_q)}, \mathbf{\Phi}_q = \bar{\phi}_q \bar{\phi}_q^H, \forall q$
18:      Set $q^\star = \arg\max_q z(\mathbf{\Phi}_q), \bar{\phi}^\star = \bar{\phi}_{q^\star}$
19: **End If**
20: Set $\theta_l^\star = \arg(\bar{\phi}_l^\star/\bar{\phi}_{L+1}^\star), \forall l, \phi^\star = [e^{j\theta_1^\star}, \ldots, e^{j\theta_L^\star}]^H$
21: **Output** $\phi^\star$

---

phase shift of element l is retrieved by $\theta_l^\star = \arg(\bar{\phi}_l^\star/\bar{\phi}_{L+1}^\star)$. Problem (25) after rank relaxation can be solved by existing optimization tools such as CVX [39]. The SCA algorithm of passive beamforming is summarized in Algorithm 1.

Proposition 1. *For any feasible initial point, the proposed SCA Algorithm 1 can provide a local optimal $\mathbf{\Phi}^\star$ that satisfies the KKT conditions, although there is no guarantee $\mathbf{\Phi}^\star$ is rank-1.*

Proof. The objective function (25a) is non-decreasing over iterations because the solution of problem (25) at iteration $i-1$ is still a feasible point at iteration i. Moreover, the sequence $\{\tilde{z}(\mathbf{\Phi}^{(i)})\}_{i=1}^{\infty}$ is bounded above due to the unit-modulus constraint (25c). Thus, Algorithm 1 is guaranteed to converge. To prove $\mathbf{\Phi}^{(i)}$ converges to stationary points, we notice that the SCA-based Algorithm 1 is indeed an inner approximation algorithm [40], since $\tilde{z}(\mathbf{\Phi}) \leq z(\mathbf{\Phi})$, $\partial\tilde{z}(\mathbf{\Phi}^{(i)})/\partial\mathbf{\Phi} = \partial z(\mathbf{\Phi}^{(i)})/\partial\mathbf{\Phi}$ and the approximation (21) – (23) are asymptotically tight as $i \to \infty$ [41]. Therefore, Algorithm 1 is guaranteed to provide a local optimal $\mathbf{\Phi}^\star$ that satisfies the KKT conditions. $\square$

$$\begin{aligned} \tilde{z}(\mathbf{\Phi}^{(i)}) = &\frac{1}{2}\beta_2 \rho (t_{\text{I},0}^{(i)} + t_{\text{P},0}^{(i)}) \\ &+ \frac{3}{8}\beta_4 \rho^2 \left(4t_{\text{I},0}^{(i)} t_{\text{I},0}^{(i-1)} - 2(t_{\text{I},0}^{(i-1)})^2 + \sum_{k=-N+1}^{N-1} 2\Re\left\{ t_{\text{P},k}^{(i)}(t_{\text{P},k}^{(i-1)})^* \right\} - t_{\text{P},k}^{(i-1)}(t_{\text{P},k}^{(i-1)})^* \right) \\ &+ \frac{3}{2}\beta_4 \rho^2 \left(\frac{1}{2}(t_{\text{I},0}^{(i)} + t_{\text{P},0}^{(i)})(t_{\text{I},0}^{(i-1)} + t_{\text{P},0}^{(i-1)}) - \frac{1}{4}(t_{\text{I},0}^{(i-1)} + t_{\text{P},0}^{(i-1)})^2 - \frac{1}{4}(t_{\text{I},0}^{(i)} - t_{\text{P},0}^{(i)})^2 \right). \end{aligned} \qquad (24)$$

B. Active Beamforming

In the single-user scenario, the global optimal information and power precoders coincide at MRT. To prove this, we decouple the waveform in the spatial and frequency domains by

$$\boldsymbol{w}_{\mathrm{I/P},n} = s_{\mathrm{I/P},n} \boldsymbol{b}_{\mathrm{I/P},n} \tag{26}$$

where $s_{\mathrm{I/P},n}$ denotes the amplitude of modulated/multisine waveform at tone n, and $\boldsymbol{b}_{\mathrm{I/P},n}$ denotes the information/power precoder. Define $\boldsymbol{s}_{\mathrm{I/P}} \triangleq [s_{\mathrm{I/P},1}, \ldots, s_{\mathrm{I/P},N}]^T \in \mathbb{C}^{N \times 1}$ and $\boldsymbol{b}_{\mathrm{I/P}} \triangleq [\boldsymbol{b}_{\mathrm{I/P},1}^T, \ldots, \boldsymbol{b}_{\mathrm{I/P},N}^T]^T \in \mathbb{C}^{MN \times 1}$ for simplicity. The MRT precoder at subband n is given by

$$\boldsymbol{b}_{\mathrm{I/P},n}^{\star} = \frac{\boldsymbol{h}_n}{\|\boldsymbol{h}_n\|} \tag{27}$$

From the perspective of communications, the MRT precoder maximizes $|\boldsymbol{h}_n^H \boldsymbol{w}_{\mathrm{I},n}| = \|\boldsymbol{h}_n\| s_{\mathrm{I},n}$ thus maximizes rate (8). From the perspective of energy harvesting, the MRT precoder maximizes $(\boldsymbol{h}_n^H \boldsymbol{w}_{\mathrm{I/P},n})(\boldsymbol{h}_n^H \boldsymbol{w}_{\mathrm{I/P},n})^* = \|\boldsymbol{h}_n\|^2 s_{\mathrm{I/P},n}^2$ thus maximizes the second and fourth order DC terms $(11) - (14)$. Hence, MRT is the global optimal active precoder and no dedicated energy beams are required in the single-user SWIPT.

C. Waveform and Splitting Ratio

Next, we jointly optimize the waveform amplitude $\boldsymbol{s}_{\mathrm{I/P}}$ and the splitting ratio ρ for any given IRS phase shift ϕ and active precoder $\boldsymbol{b}_{\mathrm{I/P}}$. On top of (27), the equivalent channel strength at subband n is $\|\boldsymbol{h}_n\|$ and the power allocated to the modulated/multisine waveform is $s_{\mathrm{I/P},n}^2$. Hence, rate (8) reduces to

$$R(\boldsymbol{s}_{\mathrm{I}}, \rho) = \log_2 \prod_{n=1}^{N} \left(1 + \frac{(1-\rho)\|\boldsymbol{h}_n\|^2 s_{\mathrm{I},n}^2}{\sigma_n^2} \right) \tag{28}$$

and DC current (10) reduces to (29), so that problem (16) boils down to

$$\max_{\boldsymbol{s}_{\mathrm{I}}, \boldsymbol{s}_{\mathrm{P}}, \rho} \quad z(\boldsymbol{s}_{\mathrm{I}}, \boldsymbol{s}_{\mathrm{P}}, \rho) \tag{30a}$$

$$\text{s.t.} \quad \frac{1}{2} \left(\|\boldsymbol{s}_{\mathrm{I}}\|^2 + \|\boldsymbol{s}_{\mathrm{P}}\|^2 \right) \le P, \tag{30b}$$

$$R(\boldsymbol{s}_{\mathrm{I}}, \rho) \ge \bar{R}. \tag{30c}$$

Following [14], we introduce auxiliary variables $t'', \bar{\rho}$ and transform it into a reversed GP

$$\min_{\boldsymbol{s}_{\mathrm{I}}, \boldsymbol{s}_{\mathrm{P}}, \rho, \bar{\rho}, t''} \quad \frac{1}{t''} \tag{31a}$$

$$\text{s.t.} \quad \frac{1}{2} \left(\|\boldsymbol{s}_{\mathrm{I}}\|^2 + \|\boldsymbol{s}_{\mathrm{P}}\|^2 \right) \le P, \tag{31b}$$

$$\frac{t''}{z(\boldsymbol{s}_{\mathrm{I}}, \boldsymbol{s}_{\mathrm{P}}, \rho)} \le 1, \tag{31c}$$

$$\frac{2^{\bar{R}}}{\prod_{n=1}^{N} \left(1 + \bar{\rho} \|\boldsymbol{h}_n\|^2 s_{\mathrm{I},n}^2 / \sigma_n^2 \right)} \le 1, \tag{31d}$$

$$\rho + \bar{\rho} \le 1. \tag{31e}$$

The denominators of (31c), (31d) are posynomials [42] which can be decomposed as sums of monomials

$$z(\boldsymbol{s}_{\mathrm{I}}, \boldsymbol{s}_{\mathrm{P}}, \rho) \triangleq \sum_{m_{\mathrm{P}}} g_{m_{\mathrm{P}}}(\boldsymbol{s}_{\mathrm{I}}, \boldsymbol{s}_{\mathrm{P}}, \rho), \tag{32}$$

$$1 + \frac{\bar{\rho} \|\boldsymbol{h}_n\|^2 s_{\mathrm{I},n}^2}{\sigma_n^2} \triangleq \sum_{m_{\mathrm{I},n}} g_{m_{\mathrm{I},n}}(s_{\mathrm{I},n}, \bar{\rho}) \tag{33}$$

where $m_{\mathrm{P}} = (2N^3 + 6N^2 + 7N)/3$ and $m_{\mathrm{I},n} = 2$. We then upper bound (32) and (33) by Arithmetic Mean-Geometric Mean (AM-GM) inequality [43] and transform problem (31) to

$$\min_{\boldsymbol{s}_{\mathrm{I}}, \boldsymbol{s}_{\mathrm{P}}, \rho, \bar{\rho}, t''} \quad \frac{1}{t''} \tag{34a}$$

$$\text{s.t.} \quad \frac{1}{2} \left(\|\boldsymbol{s}_{\mathrm{I}}\|^2 + \|\boldsymbol{s}_{\mathrm{P}}\|^2 \right) \le P, \tag{34b}$$

$$t'' \prod_{m_{\mathrm{P}}} \left(\frac{g_{m_{\mathrm{P}}}(\boldsymbol{s}_{\mathrm{I}}, \boldsymbol{s}_{\mathrm{P}}, \rho)}{\gamma_{m_{\mathrm{P}}}} \right)^{-\gamma_{m_{\mathrm{P}}}} \le 1, \tag{34c}$$

$$2^{\bar{R}} \prod_{n} \prod_{m_{\mathrm{I},n}} \left(\frac{g_{m_{\mathrm{I},n}}(s_{\mathrm{I},n}, \bar{\rho})}{\gamma_{m_{\mathrm{I},n}}} \right)^{-\gamma_{m_{\mathrm{I},n}}} \le 1, \tag{34d}$$

$$\rho + \bar{\rho} \le 1 \tag{34e}$$

where $\gamma_{m_{\mathrm{P}}}, \gamma_{m_{\mathrm{I},n}} \ge 0$, $\sum_{m_{\mathrm{P}}} \gamma_{m_{\mathrm{P}}} = \sum_{m_{\mathrm{I},n}} \gamma_{m_{\mathrm{I},n}} = 1$. The tightness of the AM-GM inequality depends on $\{\gamma_{m_{\mathrm{P}}}, \gamma_{m_{\mathrm{I},n}}\}$ that require successive update [14], and a feasible choice at iteration i is

$$\gamma_{m_{\mathrm{P}}}^{(i)} = \frac{g_{m_{\mathrm{P}}}(\boldsymbol{s}_{\mathrm{I}}^{(i-1)}, \boldsymbol{s}_{\mathrm{P}}^{(i-1)}, \rho^{(i-1)})}{z(\boldsymbol{s}_{\mathrm{I}}^{(i-1)}, \boldsymbol{s}_{\mathrm{P}}^{(i-1)}, \rho^{(i-1)})}, \tag{35}$$

$$\gamma_{m_{\mathrm{I},n}}^{(i)} = \frac{g_{m_{\mathrm{I},n}}(s_{\mathrm{I},n}^{(i-1)}, \bar{\rho}^{(i-1)})}{1 + \bar{\rho}^{(i-1)} \|\boldsymbol{h}_n\|^2 (s_{\mathrm{I},n}^{(i-1)})^2 / \sigma_n^2}. \tag{36}$$

$$z(\boldsymbol{s}_{\mathrm{I}}, \boldsymbol{s}_{\mathrm{P}}, \rho) = \frac{1}{2}\beta_2 \rho \sum_{n=1}^{N} \|\boldsymbol{h}_n\|^2 (s_{\mathrm{I},n}^2 + s_{\mathrm{P},n}^2) + \frac{3}{8}\beta_4 \rho^2 \left(2 \sum_{n_1, n_2} \prod_{j=1}^{2} \|\boldsymbol{h}_{n_j}\|^2 s_{\mathrm{I},n_j}^2 + \sum_{\substack{n_1, n_2, n_3, n_4 \\ n_1 + n_2 = n_3 + n_4}} \prod_{j=1}^{4} \|\boldsymbol{h}_{n_j}\| s_{\mathrm{P},n_j} \right)$$

$$+ \frac{3}{2}\beta_4 \rho^2 \left(\sum_{n_1, n_2} \|\boldsymbol{h}_{n_1}\|^2 \|\boldsymbol{h}_{n_2}\|^2 s_{\mathrm{I},n_1}^2 s_{\mathrm{P},n_2}^2 \right). \tag{29}$$

Algorithm 2 GP: Waveform Amplitude and Splitting Ratio.

1: **Input** $\beta_2, \beta_4, \boldsymbol{h}_n, P, \sigma_n, \bar{R}, \epsilon, \forall n$
2: **Initialize** $i \leftarrow 0, \boldsymbol{s}_{\mathrm{I/P}}^{(0)}, \rho^{(0)}$
3: **Repeat**
4:      $i \leftarrow i + 1$
5:      Update $\{\gamma_{m_\mathrm{P}}^{(i)}, \gamma_{m_{\mathrm{I},n}}^{(i)}\}, \forall n$ by (35), (36)
6:      Get $\boldsymbol{s}_{\mathrm{I/P}}^{(i)}, \rho^{(i)}$ by solving problem (34)
7:      Compute $z^{(i)}$ by (29)
8: **Until** $|z^{(i)} - z^{(i-1)}| \leq \epsilon$
9: Set $\boldsymbol{s}_{\mathrm{I/P}}^\star = \boldsymbol{s}_{\mathrm{I/P}}^{(i)}, \rho^\star = \rho^{(i)}$
10: **Output** $\boldsymbol{s}_\mathrm{I}^\star, \boldsymbol{s}_\mathrm{P}^\star, \rho^\star$

Algorithm 3 BCD: Waveform, Beamforming and Splitting Ratio.

1: **Input** $\beta_2, \beta_4, \boldsymbol{h}_{\mathrm{D},n}, \boldsymbol{V}_n, P, \sigma_n, \bar{R}, Q, \epsilon, \forall n$
2: **Initialize** $i \leftarrow 0, \boldsymbol{\phi}^{(0)}, \boldsymbol{b}_{\mathrm{I/P}}^{(0)}, \boldsymbol{s}_{\mathrm{I/P}}^{(0)}, \rho^{(0)}$
3: Get $\boldsymbol{w}_{\mathrm{I/P},n}^{(0)}, \forall n$ by (26)
4: **Repeat**
5:      $i \leftarrow i + 1$
6:      Get $\boldsymbol{\phi}^{(i)}$ based on $\boldsymbol{w}_{\mathrm{I/P}}^{(i-1)}, \rho^{(i-1)}$ by Algorithm 1
7:      Update $\boldsymbol{h}_n^{(i)}, \forall n$ by (5)
8:      Get $\boldsymbol{s}_{\mathrm{I/P}}^{(i)}, \rho^{(i)}$ based on $\boldsymbol{h}_n^{(i)}, \forall n$ by Algorithm 2
9:      Update $\boldsymbol{w}_{\mathrm{I/P},n}^{(i)}, \forall n$ by (26)
10:      Compute $z^{(i)}$ by (29)
11: **Until** $|z^{(i)} - z^{(i-1)}| \leq \epsilon$
12: Set $\boldsymbol{\phi}^\star = \boldsymbol{\phi}^{(i)}, \boldsymbol{w}_{\mathrm{I/P}}^\star = \boldsymbol{w}_{\mathrm{I/P}}^{(i)}, \rho^\star = \rho^{(i)}$
13: **Output** $\boldsymbol{\phi}^\star, \boldsymbol{w}_\mathrm{I}^\star, \boldsymbol{w}_\mathrm{P}^\star, \rho^\star$

$\boldsymbol{s}_\mathrm{I}, \boldsymbol{s}_\mathrm{P}, \rho$ are updated iteratively until convergence. Problem (34) can be solved by existing optimization tools such as CVX [39]. The GP algorithm of joint waveform amplitude and splitting ratio optimization is summarized in Algorithm 2.

Proposition 2. *For any feasible initial point, the GP Algorithm 2 is guaranteed to converge to a local optimal point of the waveform amplitude and splitting ratio problem* (30).

Proof. See [8], [14]. $\qquad\square$

D. Block Coordinate Descent

Based on the CSIT of direct and cascaded channels, we iteratively update the passive beamforming ϕ by Algorithm 1, the active beamforming $\boldsymbol{b}_{\mathrm{I/P},n}, \forall n$ by equation (27), and the waveform amplitude $\boldsymbol{s}_{\mathrm{I/P}}$ and splitting ratio ρ by Algorithm 2, until convergence. The BCD algorithm is summarized in Algorithm 3.

Proposition 3. *Suppose $\boldsymbol{\Phi}$ is rank-1, every limit point $(\boldsymbol{\phi}^\star, \boldsymbol{w}_\mathrm{I}^\star, \boldsymbol{w}_\mathrm{P}^\star, \rho^\star)$ provided by the BCD Algorithm 3 is a local optimal point of the original problem* (16).

Proof. The objective function (16a) is non-decreasing over iterations of Algorithm 3, which is also upper-bounded due to the unit-modulus constraint (16d) and the transmit power constraint (16b). If $\boldsymbol{\Phi}$ is rank-1, then ϕ can be extracted without performance loss and strict convergence of Algorithm 3 is

guaranteed. As demonstrated in [44], the limit point obtained by alternatively updating $\phi, \boldsymbol{b}_{\mathrm{I/P}}, \boldsymbol{s}_{\mathrm{I/P}}$ and ρ via BCD is a local optimal solution of problem (16). $\qquad\square$

E. Low-Complexity Adaptive Design

The GP Algorithm 2 achieves local optimality at a cost of exponential computational complexity [43]. To facilitate practical SWIPT implementation, we propose two low-complexity waveform amplitude design by combining WF and SMF under TS and PS setups. The optimal waveform design for WIT corresponds to the WF strategy that assigns the amplitude of modulated tone n by

$$s_{\mathrm{I},n} = \sqrt{2\left(\mu - \frac{\sigma_n^2}{P\|\boldsymbol{h}_n\|^2}\right)^+} \qquad (37)$$

where μ is chosen to satisfy the power constraint $\|\boldsymbol{s}_I\|^2/2 \leq P$. The closed-form solution can be obtained by iterative power allocation [45] and the details are omitted here. On the other hand, SMF was proposed in [12] as a suboptimal WPT resource allocation scheme that assigns the amplitude of sinewave n by

$$s_{\mathrm{P},n} = \sqrt{\frac{2P}{\sum_{n=1}^N \|\boldsymbol{h}_n\|^{2\alpha}}}\|\boldsymbol{h}_n\|^\alpha \qquad (38)$$

where the scaling ratio $\alpha \geq 1$ scales the matched filter to exploit the rectifier nonlinearity. In the low-complexity TS waveform design, modulated waveform (37) is used in the data session while multisine waveform (38) is used in the energy session. In contrast, the low-complexity PS scheme jointly designs the waveform balancing ratio δ and splitting ratio ρ, and the amplitude of modulated and multisine components are given by

$$s_{\mathrm{I},n} = \sqrt{2(1-\delta)\left(\mu - \frac{\sigma_n^2}{P\|\boldsymbol{h}_n\|^2}\right)^+} \qquad (39)$$

$$s_{\mathrm{P},n} = \sqrt{\frac{2\delta P}{\sum_{n=1}^N \|\boldsymbol{h}_n\|^{2\alpha}}}\|\boldsymbol{h}_n\|^\alpha \qquad (40)$$

Besides, minor modifications are required for passive beamforming to cooperate with the low-complexity waveform schemes. To achieve the WIT point ($\eta = \rho = 0$), the achievable rate (19) instead of the DC current (24) should be maximized. To achievable non-WIT points, the rate constraint (25b) should be dropped as the R-E region is now characterized by varying η, δ and ρ. Algorithm 4 summarizes the modified passive beamforming design under low-complexity PS setup.

Similar to Algorithm 3, we propose a Low-Complexity-BCD (LC-BCD) algorithm that iteratively update the passive beamforming ϕ by Algorithm 4, the active beamforming $\boldsymbol{b}_{\mathrm{I/P},n}, \forall n$ by equation (27), and the waveform amplitude $\boldsymbol{s}_{\mathrm{I/P}}$ by (37), (38) for TS or (39), (40) for PS, until convergence. Similar to Proposition 3, strict convergence and local optimality of the LC-BCD algorithm are guaranteed if $\boldsymbol{\Phi}$ is rank-1.

Algorithm 4 Modified: IRS Phase Shift.

1: **Input** $\beta_2, \beta_4, \boldsymbol{h}_{\mathrm{D},n}, \boldsymbol{V}_n, \boldsymbol{w}_{\mathrm{I/P},n}, \rho, \sigma_n, Q, \epsilon, \forall n$
2: Construct $\boldsymbol{V}, \boldsymbol{M}, \boldsymbol{M}_n, \boldsymbol{C}_n, \boldsymbol{C}_{\mathrm{I/P},k}, \forall n, k$
3: **Initialize** $i \leftarrow 0, \boldsymbol{\Phi}^{(0)}$
4: **If** $\rho = 0$ **Then**
5:      Get $\boldsymbol{\Phi}^\star$ by maximizing (19) w.r.t. (25c), (25d)
6: **Else**
7:      **Repeat**
8:        $i \leftarrow i + 1$
9:        Set $\bar{R} = 0$
10:        Get $\boldsymbol{\Phi}^{(i)}$ by solving 25a – 25d
11:        Update $t_{\mathrm{I/P},k}^{(i)}, \forall k$ by (18)
12:        Compute $z^{(i)}$ by (20)
13:      **Until** $|z^{(i)} - z^{(i-1)}| \le \epsilon$
14:      Set $\boldsymbol{\Phi}^\star = \boldsymbol{\Phi}^{(i)}$
15: **End If**
16: **If** $\mathrm{rank}(\boldsymbol{\Phi}^\star) = 1$ **Then**
17:      Get $\bar{\phi}^\star$ by eigen decomposition, $\boldsymbol{\Phi}^\star = \bar{\phi}^\star (\bar{\phi}^\star)^H$
18: **Else**
19:      Get $\boldsymbol{U}, \boldsymbol{\Lambda}$ by eigen decomposition, $\boldsymbol{\Phi}^\star = \boldsymbol{U}\boldsymbol{\Lambda}\boldsymbol{U}^H$
20:      Generate $\boldsymbol{\xi}_q \sim \mathcal{CN}(\boldsymbol{0}, \boldsymbol{I}_{L+1}), \forall q$
21:      Construct $\bar{\phi}_q = e^{j \arg(\boldsymbol{U}\boldsymbol{\Lambda}^{1/2}\boldsymbol{\xi}_q)}, \boldsymbol{\Phi}_q = \bar{\phi}_q \bar{\phi}_q^H, \forall q$
22:      Set $q^\star = \arg\max_q R(\boldsymbol{\Phi}_q)$ or $q^\star = \arg\max_q z(\boldsymbol{\Phi}_q)$, $\bar{\phi}^\star = \bar{\phi}_{q^\star}$
23: **End If**
24: Set $\theta_l^\star = \arg(\bar{\phi}_l^\star / \bar{\phi}_{L+1}^\star), \forall l, \boldsymbol{\phi}^\star = [e^{j\theta_1^\star}, \ldots, e^{j\theta_L^\star}]^H$
25: **Output** $\boldsymbol{\phi}^\star$

(a) R-E region   (b) WPT waveform amplitude

Fig. 5. Average R-E region and WPT waveform amplitude versus N for $M = 1, L = 20, \sigma_n^2 = -40\,\mathrm{dBm}, B = 1\,\mathrm{MHz}$ and $d_\mathrm{H} = d_\mathrm{V} = 2\,\mathrm{m}$.
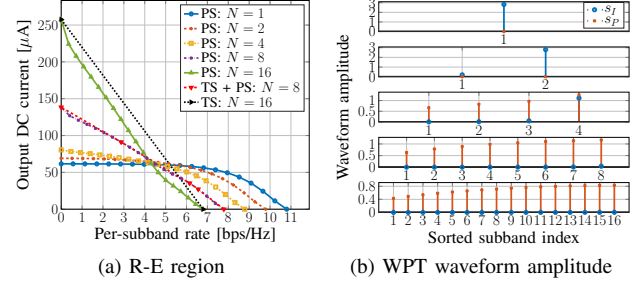

Fig. 4. System layout in simulation.

IV. PERFORMANCE EVALUATIONS

To evaluate the performance of the proposed IRS-aided SWIPT system, we consider the layout in Fig. 4 where the IRS moves along a horizontal line parallel to the AP-UE path. Let $d_\mathrm{H}, d_\mathrm{V}$ be the horizontal and vertical distances from the AP to the IRS, and denote respectively $d_\mathrm{D}, d_\mathrm{I} = \sqrt{d_\mathrm{H}^2 + d_\mathrm{V}^2}$, $d_\mathrm{R} = \sqrt{(d_\mathrm{D} - d_\mathrm{H})^2 + d_\mathrm{V}^2}$ as the distance of direct, incident and reflective links. Consider a large open space Wi-Fi-like environment at center frequency $5.18\,\mathrm{GHz}$, where the fading parameters follow IEEE TGn channel model D [46] and the reference path loss is $-35\,\mathrm{dB}$ at $1\,\mathrm{m}$. All channels are assumed NLoS with taps modelled as i.i.d. CSCG random variables of unit average sum-power, corresponding to a normalized multipath response. Rectenna parameters are chosen as $k_2 = 0.0034, k_4 = 0.3829, R_\mathrm{A} = 50\,\Omega$ such that $\beta_2 = 0.17$ and $\beta_4 = 957.25$. The average Effective Isotropic Radiated Power (EIRP) is fixed to $P = 36\,\mathrm{dBm}$ and the receive antenna gain is set to $2\,\mathrm{dBi}$. For the algorithms, the number of candidates for Gaussian randomization is $Q = 10^3$, the scaling ratio is $\alpha = 2$, the tolerance is $\epsilon = 10^{-8}$, and we assume $\delta = \rho$ for simplicity. All R-E regions are averaged over 300 channel realizations,

and the x-axis is normalized to per-subband rate R/N.

We first provide numerical proof on the strict convergence (thus local optimality) of both BCD algorithms. Too see this, we define the eigen ratio as $\nu = \max_l \lambda_l(\boldsymbol{\Phi}) / \sum_l \lambda_l(\boldsymbol{\Phi})$ where $\lambda_l(\boldsymbol{\Phi})$ is the l-th eigenvalue of $\boldsymbol{\Phi}$. $\nu = 1$ means $\boldsymbol{\Phi}$ is rank-1, and we claim $\boldsymbol{\Phi}$ is approximately rank-1 when $1 - \nu \approx 0$. Table I shows the maximum value of $1 - \nu$ over all R-E samples during both BCD algorithms. With reasonable precision, we conclude that $\boldsymbol{\Phi}$ is always rank-1 under different configurations for all tested channel realizations. It suggests that the rank constraint 25e can be dropped without performance loss, $\bar{\phi}$ can be directly obtained through eigen decomposition, and the assumption of Proposition 3 always hold such that both BCD algorithms converge to local optimal.

Fig. 5a illustrates the average R-E region versus the number of subband N. *First*, it is observed that increasing N reduces the per-subband rate R/N but boosts the harvested energy. The reason is that the power budget is divided into smaller portions for each subband, but the number of balanced DC terms m_P is increased to boost the output DC current, confirming the scaling laws in [14]. Sorted waveform amplitudes in Fig. 5b also confirmed that, from the perspective of WPT, a dedicated multisine waveform is unnecessary for a small N but is required for a large N. As shown in (12) and (14), the only difference between modulated and unmodulated waveform on z exists in the fourth-order terms, where $\mathbb{E}\left\{\mathbb{A}\left\{y_\mathrm{I}^4(t)\right\}\right\}$ has N^2 monomials with a modulation gain of 2 and $\mathbb{A}\left\{y_\mathrm{P}^4(t)\right\}$ has $(2N^3 + N)/3$ monomials without modulation gains. Therefore, the superposed waveform enlarges the R-E region for a sufficiently large N (typically no smaller than 4). *Second*, the R-E region is convex for $N = 2, 4$ and concave-convex for $N = 8, 16$. This has the consequence that PS outperforms TS for a small N and is outperformed for a large N. When N is in between, the optimal strategy is a combination of both, i.e. a time sharing between the WPT point and the saddle SWIPT point obtained by PS (as the red curve in Fig. 5a). Compared with the linear harvester model that requires no dedicated power waveform and always prefer PS, the rectifier nonlinearity enlarges the R-E region by favoring a different waveform and transceiving mode, both heavily depends on N.

The influence of the average noise power on the R-E region is investigated in Fig. 6a. *First*, we note that the R-E region is roughly concave/convex at low/high SNR such that TS/PS are preferred correspondingly. This is because the WF strategy

		M			N			L			B	
		1	2	4	1	4	16	20	40	80	1 MHz	10 MHz
max$(1-\nu)$	BCD	5.5511	6.6613	6.6613	6.6613	6.6613	6.6613	6.6613	5.5511	6.6613	6.6613	5.5511
$[\times 10^{-16}]$	LC	6.6613	6.6613	6.6613	6.6613	6.6613	6.6613	6.6613	8.8818	6.6613	6.6613	5.5511

(a) R-E region
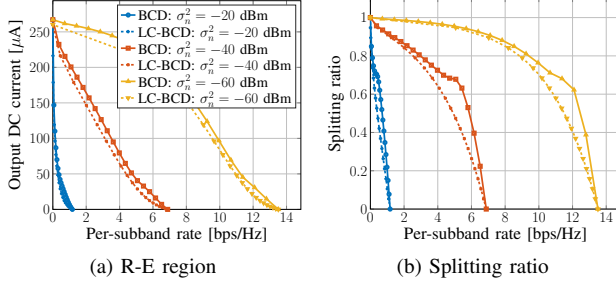
(b) Splitting ratio

Fig. 6. Average R-E region and Splitting ratio versus σ_n^2 for $M = 1$, $N = 16$, $L = 20$, $B = 1$ MHz and $d_\mathrm{H} = d_\mathrm{V} = 2$ m.

(a) R-E region

(b) WIT SNR and WPT DC current
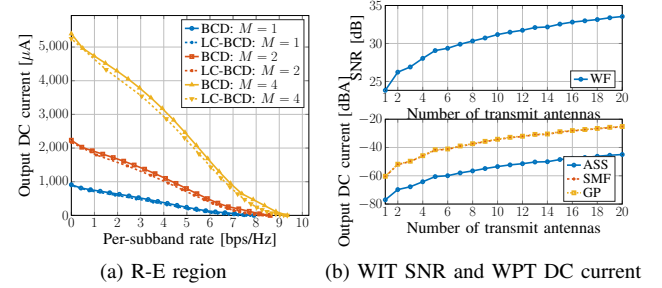
Fig. 8. Average R-E region, WIT SNR and WPT DC current versus M for $N = 16$, $L = 20$, $\sigma_n^2 = -40$ dBm, $B = 1$ MHz, $d_\mathrm{H} = d_\mathrm{V} = 0.5$ m.

(a) R-E region
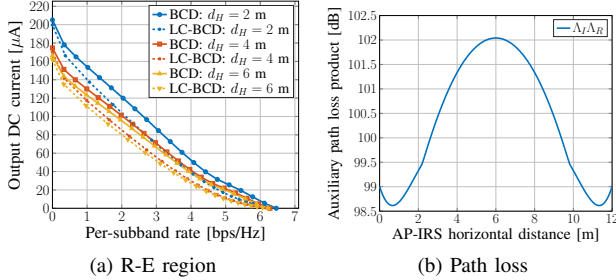
(b) Path loss

Fig. 7. Average R-E region and path loss versus d_H for $M = 1$, $N = 16$, $L = 20$, $\sigma_n^2 = -40$ dBm, $B = 1$ MHz and $d_\mathrm{V} = 2$ m.

(a) R-E region

(b) WIT SNR and WPT DC current
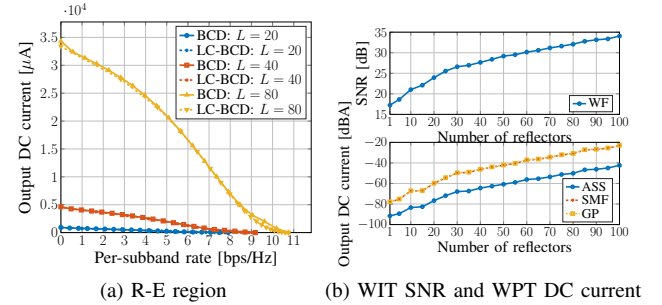
Fig. 9. Average R-E region, WIT SNR and WPT DC current versus L for $M = 1$, $N = 16$, $\sigma_n^2 = -40$ dBm, $B = 1$ MHz and $d_\mathrm{H} = d_\mathrm{V} = 0.5$ m.

tends to concentrate power on few strongest subbands at low SNR. As the rate constraint $\bar{R}$ decreases, more subbands are activated to further boost the harvested DC power thanks to the frequency compensation effect and harvester nonlinearity. *Second*, there exists a turning point in the R-E region especially for a low noise level ($\sigma_n^2 \leq -40$ dBm). The reason is that when $\bar{R}$ departs slightly from the maximum value, the algorithm tends to adjust the splitting ratio ρ rather than allocating more power to the multisine waveform, since a small-amplitude multisine could be inefficient for energy maximization. As $\bar{R}$ further decreases, a modulated waveform with a very large ρ could be outperformed by a superposed waveform with a smaller ρ, owing to the high energy efficiency of multisine. The result highlights the benefit of superposed waveform and the necessity of joint waveform and splitting ratio optimization.

In Fig. 7a, we compare the average R-E region achieved by different AP-IRS horizontal distance d_H. A *first* observation is that, different from the active Amplify-and-Forward (AF) relay with the optimal development location around the midpoint [47], placing the IRS closer to either the transmitter or the receiver would further improve the R-E tradeoff. It origins from the product-distance path loss model that applies to finite-size element reflection. As shown in Fig. 7b, although the piecewise TGn path loss model further penalizes large distance

(greater than 10 m for model D), it is still beneficial to have a short-long or long-short transmission setup, since signal attenuation increases fast at a short distance and experiences marginal effect at a long distance. On the other hand, it also suggests that developing an IRS next to the AP can effectively extend the operation range of SWIPT systems. Considering the passive characteristic of the IRS, opportunities are that it can be directly supported by the SWIPT network. A *second* observation from Fig. 7b is that there exist two optimal IRS development locations that minimize the path loss production $\Lambda_\mathrm{I} \Lambda_R$. It implies that two IRSs may be implemented to further enlarge the R-E region, one attached to the AP and one attached to the UE.

The number of transmit antennas M and IRS elements L influence the average R-E tradeoff as revealed in Fig. 8a and 9a. *First*, it is observed that adding either active or passive elements benefits both information and power transmission. This is because increasing M or L indeed enhances the equivalent composite channel strength. *Second,* the number of active and passive elements have negligible impacts on the optimal transceiving mode (TS/PS). Unlike the noise, the channel strength influences both information and power transfer, thus varying M or L simultaneously scales both rate and current and preserves the general trend of the R-E boundary. *Third,*
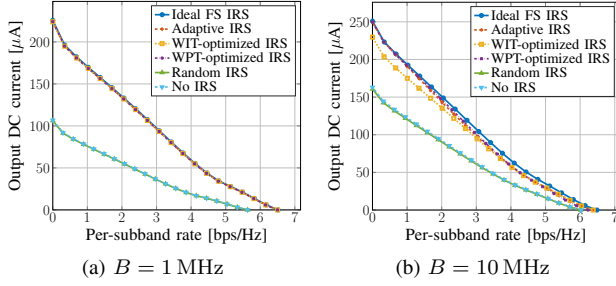
Fig. 10. Average R-E region for ideal, adaptive, fixed and no IRS versus B for $M = 1$, $N = 16$, $L = 20$, $\sigma_n^2 = -40\,\mathrm{dBm}$ and $d_\mathrm{H} = d_\mathrm{V} = 2\,\mathrm{m}$.

the passive beamforming has a larger array gain and power scaling order than the active beamforming. This behavior is more obvious in Fig. 8b and 9b that illustrate the performance of WIT and WPT only. For the active MRT beamforming, doubling M brings a $3\,\mathrm{dB}$ gain at the average output SNR, corresponding to a transmit array gain of M and a doubled harvester input power. Due to the rectifier nonlinearity, the output DC current ends up with a nearly four-time ($12\,\mathrm{dB}$) increase, validating the active scaling law in the order of M^2 [8]. On the other hand, when the IRS is very close to the transmitter or the receiver, doubling L can bring an SNR boost up to $6\,\mathrm{dB}$, corresponding to a reflect array gain of L^2. An interpretation is that the IRS coherently combines multiple signal copies with a receive array gain L, then performs an equal gain reflection with a transmit array gain L, achieving a total gain of L^2. As a consequence, doubling IRS elements brings a four-fold boost on the received signal power that further amplifies the harvested DC current by 16 times ($24\,\mathrm{dB}$), suggesting a passive scaling law in the order of L^4. Besides, by considering harvester nonlinearity, the proposed design brings a nearly $20\,\mathrm{dB}$ increase in the output DC current over the conventional linear perspective. These results emphasize the effectiveness of passive beamforming and the importance of modeling rectifier nonlinearity in the SWIPT system design. *Fourth,* small-scale SWIPT is dominated by the active beamforming while large-scale SWIPT relies more on the passive beamforming. As shown in Fig. 7b, in our setup, the direct path loss Λ_D is around $60\,\mathrm{dB}$ while the auxiliary path loss product $\Lambda_\mathrm{I}\Lambda_R$ is over $100\,\mathrm{dB}$. Hence, to fully exploit the R-E advantage of passive beamforming, a large number of reflecting elements are required to enhance the auxiliary channel strength. Another explanation is that the RF-chains of active antennas provide design flexibility in the frequency domain, while the frequency-flat characteristic of the IRS restricts its benefit for broadband transmission, especially when L is small.

Fig. 10a and 10b explore the average R-E region under different IRS configuration for narrowband transmission ($B = 1\,\mathrm{MHz}$) and broadband transmission ($B = 10\,\mathrm{MHz}$). The rate-dependent adaptive IRS strategy adjusts the passive beamforming for each point on the R-E boundary, while the WIT/WPT-based non-adaptive IRS schemes only optimize the phase shifts for information and power purposes (correspond to the points on the x and y axes, respectively). To gain some insight into the IRS behavior, we compare the results above to

no IRS and an ideal Frequency-Selective (FS) IRS. In contrast to Remark **??**, each element in the ideal FS IRS is assumed to have an independent reflection coefficient for each subband, accounting for NL variables in total. When there is only one transmit antenna, each ideal IRS element simply aligns the AP-IRS-UE channel to the AP-UE channel at all subbands, namely

$$\theta_{l,n}^\star = e^{j\arg\,(h_{\mathrm{D},n}/h_{\mathrm{I},n,l}h_{\mathrm{R},n,l})}, \quad \forall n, l. \tag{41}$$

First, it is observed that the assistance of the IRS effectively enlarges the achievable R-E region for both narrowband and broadband transmissions. *Second,* the performance of all four IRS strategies coincide with each other for narrowband SWIPT. It suggests that the optimal passive beamforming obtained for any R-E point is also optimal for the whole R-E region. Therefore, for a given channel, we can fix the active and passive beamforming, and only adapt the waveform and splitting ratio to achieve different R-E performance. This is because when the bandwidth is small, all channels are approximately flat such that the optimal ideal reflection coefficients at all subbands are approximately the same. Also, the subchannel tradeoff in Remark **??** does not exist as the auxiliary channel can be simultaneously maximized at different frequencies. *Third,* a joint optimization of waveform, active and passive beamforming, and splitting ratio is necessary to maximize the R-E tradeoff for broadband SWIPT. Recall Remark **??** that WIT and WPT prefer different subchannel strength distribution. By adaptive passive beamforming, the channel strength can either be concentrated in few strongest subbands to enhance the rate at a low SNR, or be spread evenly over all subbands to boost the output DC power. The advantage of such a smart channel control is prominent for broadband SWIPT where the strength can vary significantly for different subbands.

A. Imperfect CSIT

Due to the general lack of RF-chains at the IRS, accurate CSIT acquisition can be challenging especially for a short coherence time. Hence, we consider an imperfect CSIT model and denote the estimation of the cascaded links at subband n as

$$\hat{\boldsymbol{V}}_n = \boldsymbol{V}_n + \tilde{\boldsymbol{V}}_n \tag{42}$$

where $\tilde{\boldsymbol{V}}_n$ is the estimation error with entries in i.i.d. CSCG distribution $\mathcal{CN}(0, \epsilon_n^2)$. Perfect CSIT can be regarded as a special case with $\epsilon_n = 0$.

B. Quantized IRS

Recall in Remark 1 that one needs to vary the element impedance to adjust the reflection coefficient. To reduce the circuit complexity and control overhead, we design a passive beamforming codebook $\mathcal{C}_\phi = \{e^{j2\pi i/2^b} \mid i = 1, \ldots, 2^b\}$ to quantize each reflection coefficient by b bits.

V. Conclusion and Future Works

This paper proposes a novel IRS-aided multi-carrier downlink MISO SWIPT system to enhance the rate and energy tradeoff of a single user. We perform a joint optimization of the
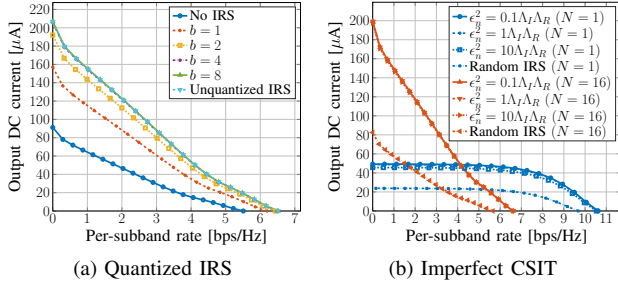
Fig. 11. Average R-E region with quantized IRS and imperfect cascaded CSIT for $M = 1$, $N = 16$, $L = 20$, $\sigma_n^2 = -40\,\mathrm{dBm}$, $B = 1\,\mathrm{MHz}$ and $d_\mathrm{H} = d_\mathrm{V} = 2\,\mathrm{m}$.

waveform and active beamforming at the transmitter, the passive beamforming at the IRS, and the splitting ratio at the receiver to enlarge the achievable R-E region. Different from the existing IRS-aided SWIPT literature, this paper leverages rectifier nonlinearity in passive beamforming design and investigates a multi-carrier transmission for practical co-localized receiver architectures. Efficient algorithms based on the BCD, SCA, SDR and GP techniques are numerically demonstrated feasible for all tested channel realizations under different configurations. We confirm that considering harvester nonlinearity, a dedicated power waveform is generally required to boost the R-E tradeoff. When developed near the transmitter, the IRS can provide effective channel enhancement to enlarge the R-E region and expand the operation range. Compared with the transmit antenna, the IRS element has no design flexibility in the frequency domain, but it integrates the coherent combining and transmission techniques in a fully passive manner to further boost the array gain and power scaling effects. Finally, the optimal passive beamforming at any R-E point is also optimal for the whole R-E region of narrowband transmission, and the rate-dependent adaptive passive beamforming is beneficial for broadband transmission.

The combination of IRS and SWIPT brings many possibilities and challenges. For example, how to optimize the waveform, active and passive beamforming in a multi-user SWIPT system? How can multiple IRS cooperate with each other to further benefit the R-E tradeoff? How to perform channel estimation without RF-chains at the IRS? How to design an IRS-aided SWIPT system for different multiple access techniques? How to develop SWIPT in new networks, such as cell-free massive Multiple-Input Multiple-Output (MIMO)? Can IRS operation be directly supported by SWIPT? Answers to these questions may bring a new wireless revolution.

REFERENCES

[1] B. Clerckx, R. Zhang, R. Schober, D. W. K. Ng, D. I. Kim, and H. V. Poor, "Fundamentals of wireless information and power transfer: From RF energy harvester models to signal and system designs," *IEEE Journal on Selected Areas in Communications*, vol. 37, no. 1, pp. 4–33, 2019.

[2] L. R. Varshney, "Transporting information and energy simultaneously," *IEEE International Symposium on Information Theory - Proceedings*, pp. 1612–1616, 2008.

[3] X. Zhou, R. Zhang, and C. K. Ho, "Wireless information and power transfer: Architecture design and rate-energy tradeoff," *IEEE Transactions on Communications*, vol. 61, no. 11, pp. 4754–4767, 2013.

[4] R. Zhang and C. K. Ho, "MIMO broadcasting for simultaneous wireless information and power transfer," *IEEE Transactions on Wireless Communications*, vol. 12, no. 5, pp. 1989–2001, 2013.

[5] J. Park and B. Clerckx, "Joint wireless information and energy transfer in a K-user MIMO interference channel," *IEEE Transactions on Wireless Communications*, vol. 13, no. 10, pp. 5781–5796, 2014.

[6] M. S. Trotter, J. D. Griffin, and G. D. Durgin, "Power-optimized waveforms for improving the range and reliability of RFID systems," *2009 IEEE International Conference on RFID, RFID 2009*, pp. 80–87, 2009.

[7] B. Clerckx and J. Kim, "On the Beneficial Roles of Fading and Transmit Diversity in Wireless Power Transfer with Nonlinear Energy Harvesting," *IEEE Transactions on Wireless Communications*, vol. 17, no. 11, pp. 7731–7743, 2018.

[8] B. Clerckx and E. Bayguzina, "Waveform Design for Wireless Power Transfer," *IEEE Transactions on Signal Processing*, vol. 64, no. 23, pp. 6313–6328, 2016.

[9] J. Kim, B. Clerckx, and P. D. Mitcheson, "Experimental Analysis of Harvested Energy and Throughput Trade-off in a Realistic SWIPT System," in *2019 IEEE Wireless Power Transfer Conference (WPTC)*. IEEE, jun 2019, pp. 1–5.

[10] ——, "Signal and System Design for Wireless Power Transfer : Prototype, Experiment and Validation," *IEEE Transactions on Wireless Communications*, vol. 1276, no. c, pp. 1–1, 2020.

[11] J. Kim and B. Clerckx, "Range Expansion for Wireless Power Transfer: A Joint Beamforming and Waveform Architecture," *arXiv preprint arXiv:2010.01680*, oct 2020.

[12] B. Clerckx and E. Bayguzina, "Low-Complexity Adaptive Multisine Waveform Design for Wireless Power Transfer," *IEEE Antennas and Wireless Propagation Letters*, vol. 16, no. 1, pp. 2207–2210, 2017.

[13] J. Kim, B. Clerckx, and P. D. Mitcheson, "Prototyping and experimentation of a closed-loop wireless power transmission with channel acquisition and waveform optimization," *WPTC 2017 - Wireless Power Transfer Conference*, pp. 1–4, 2017.

[14] B. Clerckx, "Wireless Information and Power Transfer: Nonlinearity, Waveform Design, and Rate-Energy Tradeoff," *IEEE Transactions on Signal Processing*, vol. 66, no. 4, pp. 847–862, 2018.

[15] M. Varasteh, B. Rassouli, and B. Clerckx, "On Capacity-Achieving Distributions for Complex AWGN Channels Under Nonlinear Power Constraints and Their Applications to SWIPT," *IEEE Transactions on Information Theory*, vol. 66, no. 10, pp. 6488–6508, 2020.

[16] ——, "SWIPT Signaling over Frequency-Selective Channels with a Nonlinear Energy Harvester: Non-Zero Mean and Asymmetric Inputs," *IEEE Transactions on Communications*, vol. 67, no. 10, pp. 7195–7210, 2019.

[17] M. Varasteh, J. Hoydis, and B. Clerckx, "Learning to Communicate and Energize: Modulation, Coding and Multiple Access Designs for Wireless Information-Power Transmission," *IEEE Transactions on Communications*, vol. 6778, no. DL, pp. 1–1, 2020.

[18] R. S. Anwar, L. Mao, and H. Ning, "Frequency selective surfaces: A review," *Applied Sciences (Switzerland)*, vol. 8, no. 9, pp. 1–47, 2018.

[19] T. J. Cui, M. Q. Qi, X. Wan, J. Zhao, and Q. Cheng, "Coding metamaterials, digital metamaterials and programmable metamaterials," *Light: Science & Applications*, vol. 3, no. 10, pp. e218–e218, 2014.

[20] C. Liaskos, S. Nie, A. Tsioliaridou, A. Pitsillides, S. Ioannidis, and I. Akyildiz, "Realizing Wireless Communication Through Software-Defined HyperSurface Environments," *19th IEEE International Symposium on a World of Wireless, Mobile and Multimedia Networks, WoWMoM 2018*, 2018.

[21] Q. Wu and R. Zhang, "Intelligent Reflecting Surface Enhanced Wireless Network: Joint Active and Passive Beamforming Design," in *2018 IEEE Global Communications Conference (GLOBECOM)*, vol. 18, no. 11. IEEE, dec 2018, pp. 1–6.

[22] ——, "Beamforming Optimization for Intelligent Reflecting Surface with Discrete Phase Shifts," in *ICASSP 2019 - 2019 IEEE International Conference on Acoustics, Speech and Signal Processing (ICASSP)*. IEEE, may 2019, pp. 7830–7833.

[23] ——, "Intelligent Reflecting Surface Enhanced Wireless Network via Joint Active and Passive Beamforming," *IEEE Transactions on Wireless Communications*, vol. 18, no. 11, pp. 5394–5409, nov 2019.

[24] S. Abeywickrama, R. Zhang, and C. Yuen, "Intelligent Reflecting Surface: Practical Phase Shift Model and Beamforming Optimization," in *ICC 2020 - 2020 IEEE International Conference on Communications (ICC)*. IEEE, jun 2020, pp. 1–6.

[25] Q.-U.-A. Nadeem, A. Kammoun, A. Chaaban, M. Debbah, and M.-S. Alouini, "Intelligent Reflecting Surface Assisted Wireless

Communication: Modeling and Channel Estimation," *arXiv preprint arXiv:1906.02360*, pp. 1–7, 2019.

[26] C. You, B. Zheng, and R. Zhang, "Intelligent Reflecting Surface with Discrete Phase Shifts: Channel Estimation and Passive Beamforming," in *ICC 2020 - 2020 IEEE International Conference on Communications (ICC)*.   IEEE, jun 2020, pp. 1–6.

[27] J.-M. Kang, "Intelligent Reflecting Surface: Joint Optimal Training Sequence and Refection Pattern," *IEEE Communications Letters*, vol. 24, no. 8, pp. 1784–1788, aug 2020.

[28] P. Wang, J. Fang, H. Duan, and H. Li, "Compressed Channel Estimation for Intelligent Reflecting Surface-Assisted Millimeter Wave Systems," *IEEE Signal Processing Letters*, vol. 27, pp. 905–909, 2020.

[29] Y. Yang, S. Zhang, and R. Zhang, "IRS-Enhanced OFDMA: Joint Resource Allocation and Passive Beamforming Optimization," *IEEE Wireless Communications Letters*, pp. 1–1, 2020.

[30] L. Dai, M. D. Renzo, C. B. Chae, L. Hanzo, B. Wang, M. Wang, X. Yang, J. Tan, S. Bi, S. Xu, F. Yang, and Z. Chen, "Reconfigurable Intelligent Surface-Based Wireless Communications: Antenna Design, Prototyping, and Experimental Results," *IEEE Access*, vol. 8, pp. 45 913–45 923, 2020.

[31] Q. Wu and R. Zhang, "Weighted Sum Power Maximization for Intelligent Reflecting Surface Aided SWIPT," *IEEE Wireless Communications Letters*, vol. 9, no. 5, pp. 586–590, 2020.

[32] Y. Tang, G. Ma, H. Xie, J. Xu, and X. Han, "Joint Transmit and Reflective Beamforming Design for IRS-Assisted Multiuser MISO SWIPT Systems," in *ICC 2020 - 2020 IEEE International Conference on Communications (ICC)*.   IEEE, jun 2020, pp. 1–6.

[33] Q. Wu and R. Zhang, "Joint Active and Passive Beamforming Optimization for Intelligent Reflecting Surface Assisted SWIPT Under QoS Constraints," *IEEE Journal on Selected Areas in Communications*, vol. 38, no. 8, pp. 1735–1748, aug 2020.

[34] R. C. Hansen, "Relationships Between Antennas as Scatterers and as Radiators," *Proceedings of the IEEE*, vol. 77, no. 5, pp. 659–662, 1989.

[35] M. Piñuela, P. D. Mitcheson, and S. Lucyszyn, "Ambient RF energy harvesting in urban and semi-urban environments," *IEEE Transactions on Microwave Theory and Techniques*, vol. 61, no. 7, pp. 2715–2726, 2013.

[36] Y. Huang and B. Clerckx, "Large-Scale Multiantenna Multisine Wireless Power Transfer," *IEEE Transactions on Signal Processing*, vol. 65, no. 21, pp. 5812–5827, 2017.

[37] T. Adali and S. Haykin, *Adaptive Signal Processing*.   Hoboken, NJ, USA: John Wiley & Sons, Inc., mar 2010.

[38] Z.-q. Luo, A. M.-c. So, Y. Ye, and S. Zhang, "Semidefinite Relaxation of Quadratic Optimization Problems -From its practical deployments and scope of applicability to key theoretical results-," *IEEE Signal Processing Magazine*, no. May, pp. 20–34, 2010.

[39] M. C. Grant and S. P. Boyd, "CVX: Matlab software for disciplined convex programming, version 2.0 beta," 2013. [Online]. Available: http://cvxr.com/cvx/

[40] B. R. Marks and G. P. Wright, "A General Inner Approximation Algorithm for Nonconvex Mathematical Programs," *Operations Research*, vol. 26, no. 4, pp. 681–683, 1978.

[41] W. C. Li, T. H. Chang, C. Lin, and C. Y. Chi, "Coordinated beamforming for multiuser MISO interference channel under rate outage constraints," *IEEE Transactions on Signal Processing*, vol. 61, no. 5, pp. 1087–1103, 2013.

[42] S. Boyd, S. J. Kim, L. Vandenberghe, and A. Hassibi, "A tutorial on geometric programming," *Optimization and Engineering*, vol. 8, no. 1, pp. 67–127, 2007.

[43] M. Chiang, *Geometric Programming for Communication Systems*.   now Publishers Inc, 2005, vol. 2, no. 1.

[44] L. Grippo and M. Sciandrone, "On the convergence of the block nonlinear Gauss-Seidel method under convex constraints," *Operations Research Letters*, vol. 26, no. 3, pp. 127–136, 2000.

[45] D. Tse and V. Pramod, "Fundamentals of wireless communication," *Fundamentals of Wireless Communication*, vol. 9780521845, pp. 1–564, 2005.

[46] V. Erceg, "TGn Channel Models," in *IEEE 802.11-03/940r4*, 2004.

[47] S. Li, K. Yang, M. Zhou, J. Wu, L. Song, Y. Li, and H. Li, "Full-Duplex Amplify-and-Forward Relaying: Power and Location Optimization," *IEEE Transactions on Vehicular Technology*, vol. 66, no. 9, pp. 8458–8468, 2017.